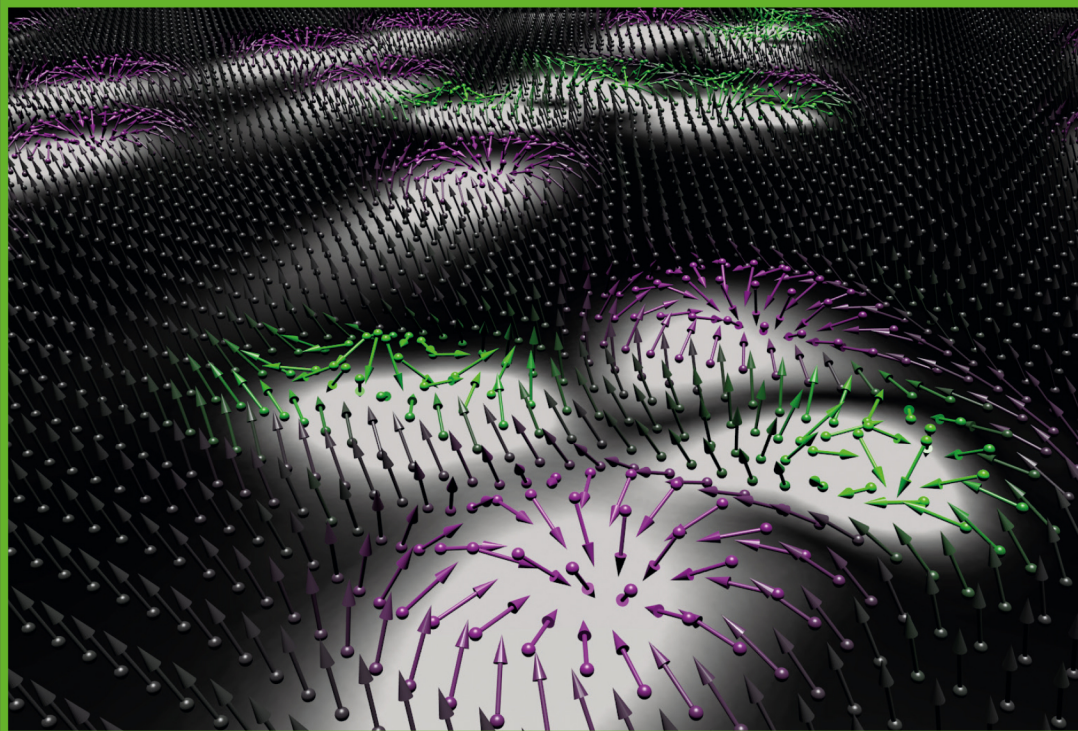


WOODHEAD PUBLISHING SERIES IN ELECTRONIC AND OPTICAL MATERIALS



# MAGNETIC SKYRMIONS AND THEIR APPLICATIONS



Edited by  
**GIOVANNI FINOCCHIO**  
**CHRISTOS PANAGOPOULOS**

# Contents

<b>Contributors</b>	<b>ix</b>
<b>Preface</b>	<b>xiii</b>
<b>Acknowledgments</b>	<b>xvii</b>
<b>1 Magnetism and topology</b>	<b>1</b>
<i>André Thiaville, Jacques Miltat, and Stanislas Rohart</i>	
1.1 Introduction	1
1.2 Topological defects in magnetism	2
1.3 Topologically stable structures (topological solitons) in magnetism	6
1.4 Effect of topology on magnetization dynamics	15
1.5 Topology versus energetic stability	19
1.6 Conclusion and perspectives	26
Acknowledgments	27
References	27
<b>2 Materials for skyrmionics</b>	<b>31</b>
<i>Kai Litzius and Mathias Kläui</i>	
2.1 Introduction	31
2.2 Overview of materials for skyrmion stabilization	33
2.3 Interface-dominated multilayer materials	38
2.4 Materials for hybrid skyrmions	43
2.5 Anisotropic DMI and antiskyrmions	44
2.6 Bilayer systems	46
2.7 Chiral bobbers	46
2.8 Materials for RKKY–DMI	47
2.9 Effect of crystallinity and annealing	47
2.10 Outlook	48
Acknowledgments	49
References	49
<b>3 Characterizing magnetic skyrmions at their fundamental length and time scales</b>	<b>55</b>
<i>Peter Fischer and Sujoy Roy</i>	
3.1 Overview of the variety of spin textures in skyrmions	55
3.2 Scientific motivation for static and dynamic studies of skyrmions	67

3.3	Features of the various probes used for imaging: Photons, electrons and scanning probes	70
3.4	Resonant X-ray and neutron scattering studies on skyrmions	77
3.5	Examples of recent research	85
3.6	Future challenges in characterizing skyrmion spin textures	92
	References	93
<b>4</b>	<b>Mapping the magnetic field of skyrmions and spin spirals by scanning probe microscopy</b>	<b>99</b>
	<i>Hans J. Hug</i>	
4.1	Introduction	99
4.2	Magnetic force microscopy methods	100
4.3	NV-center microscopy	125
	Acknowledgments	139
	References	139
<b>5</b>	<b>Scanning probe microscopy methods for imaging skyrmions and spin spirals with atomic resolution</b>	<b>143</b>
	<i>Hans J. Hug</i>	
5.1	Introduction	143
5.2	Scanning tunneling microscopy methods	145
5.3	Magnetic exchange force microscopy	170
	Acknowledgments	176
	References	177
	Further reading	180
<b>6</b>	<b>Static properties of magnetic skyrmions</b>	<b>181</b>
	<i>Roberto Zivieri and Oksana Chubykalo-Fesenko</i>	
6.1	Introduction	181
6.2	Micromagnetic model	183
6.3	Analytical model for Néel skyrmion energy calculation	184
6.4	3D skyrmion diameters distribution	186
6.5	2D model for the skyrmion diameters distribution	201
6.6	Numerical results	206
6.7	Conclusions	226
	Acknowledgments	227
	References	227
<b>7</b>	<b>Dynamics of magnetic skyrmions</b>	<b>233</b>
	<i>Riccardo Tomasello, Luis Sánchez-Tejerina, and Mario Carpentieri</i>	
7.1	Skyrmion shifting	233
7.2	Dynamical skyrmion and oscillations	244
7.3	Resonant modes of skyrmions and application to study their fundamental time scales	247
7.4	Implications and perspectives on applications	248
	References	249

<b>8</b>	<b>Electrical nucleation and detection of magnetic skyrmions</b>	<b>255</b>
	<i>Felix Büttner and William Legrand</i>	
8.1	Isolated skyrmions	255
8.2	Electrical nucleation of magnetic skyrmions	256
8.3	Electrical detection of magnetic skyrmions	266
8.4	Scalability	277
	References	278
<b>9</b>	<b>Topological Hall effect</b>	<b>289</b>
	<i>Igor Rozhansky and Konstantin Denisov</i>	
9.1	Anomalous and topological Hall effects	289
9.2	Adiabatic theory of the THE	290
9.3	Topological Hall effect in the weak-coupling regime	297
9.4	Topological Hall effect in a general case	302
	References	311
<b>10</b>	<b>Skyrmions in ferrimagnets</b>	<b>315</b>
	<i>Xichao Zhang, Yan Zhou, and Seonghoon Woo</i>	
10.1	Ferrimagnetic skyrmions: Topological properties and materials	315
10.2	Imaging, writing, deleting, and electrical detection of ferrimagnetic skyrmions	319
10.3	Current-induced dynamics of ferrimagnetic skyrmions	322
10.4	Potential applications of ferrimagnetic skyrmions	325
10.5	Summary	327
	Acknowledgments	328
	References	328
<b>11</b>	<b>Skyrmions in antiferromagnets</b>	<b>333</b>
	<i>Oleg A. Tretiakov</i>	
11.1	Introduction	333
11.2	Antiferromagnetic materials for skyrmions	333
11.3	Statics of antiferromagnetic skyrmion	334
11.4	Dynamics of antiferromagnetic skyrmion	336
11.5	Bimerons in antiferromagnets	339
11.6	Potential applications of antiferromagnetic skyrmions	340
11.7	Conclusions and outlook	342
	References	343
<b>12</b>	<b>Multiple skyrmionic states and oblique spirals in bulk cubic helimagnets</b>	<b>347</b>
	<i>Andrey O. Leonov and Catherine Pappas</i>	
12.1	Introduction	347
12.2	Phenomenological theory of modulated states in chiral helimagnets	348

12.3	Rich behavior of spiral states in helimagnets with cubic anisotropy	350
12.4	Skyrmion stability by means of cubic anisotropy	359
12.5	Conclusions	364
	References	364
<b>13</b>	<b>Conventional applications of skyrmions</b>	<b>367</b>
	<i>Xichao Zhang, Jing Xia, Laichuan Shen, Motohiko Ezawa, Xiaoxi Liu, and Yan Zhou</i>	
13.1	Introduction	367
13.2	Skyrmion-based racetrack memory	368
13.3	Skyrmion-based logic computing gates	374
13.4	Skyrmion-based nano-oscillator devices	378
13.5	Skyrmion-based transistor-like functional devices	381
13.6	Electric field control of skyrmion for future applications	383
13.7	Summary	384
	Acknowledgments	385
	References	385
<b>14</b>	<b>Unconventional applications of skyrmions</b>	<b>393</b>
	<i>Wang Kang, Sai Li, Xing Chen, Daoqian Zhu, Xueying Zhang, Na Lei, and Weisheng Zhao</i>	
14.1	Skyrmion-based memristors and neuromorphic computing	393
14.2	Skyrmion for stochastic computing	399
14.3	Skyrmion for reservoir computing	403
14.4	Skyrmions for Boolean logic computing gates	407
14.5	Challenges and perspectives	412
	References	413
	Further reading	416
<b>15</b>	<b>Introduction to topology</b>	<b>417</b>
	<i>Gabriele Bonanno and Giuseppina D'Agù</i>	
15.1	Topological spaces	417
15.2	Metric spaces	424
15.3	Connected sets	426
15.4	Compact sets	429
15.5	Homotopy theory	430
15.6	Winding numbers	432
15.7	Applications of windings numbers	435
15.8	Conclusions	438
	Further reading	439
	<b>Index</b>	<b>441</b>

# Preface

This book discusses fundamental concepts and research activities in the rapidly growing field of magnetic skyrmions. These are particle-like objects that are topologically stable, highly mobile, and have the smallest magnetic configurations, making them promising for technological applications, including spintronics and neuromorphic computing.

Paradoxically, skyrmions were expected to be short-time excitations, quickly collapsing into point or linear singularities. However, the seminal work of A.N. Bogdanov and D.N. Yablonsky in 1989 indicated skyrmions may exist as long-living metastable configurations in low-symmetry condensed matter systems with broken mirror symmetry. For example, in noncentrosymmetric magnetic materials, the underlying crystallographic handedness imposes a unique stabilization mechanism (Dzyaloshinskii-Moriya interaction) for two- and three-dimensional localized states. Hence, material classes expected to host skyrmions may include noncentrosymmetric ferro- and antiferromagnets and multiferroics where the topological field is the magnetization. A similar stabilization mechanism for chiral skyrmions may apply in liquid crystals and ferroelectrics.

Expectedly, the scientific and technological relevance of chiral skyrmions is fueling research in novel classes of materials. Magnetic skyrmions have been reported in a plethora of materials, including bulk ferromagnets, ferrimagnets, and multiferroics. Furthermore, one can engineer a structure that cannot be inverted. For example, by breaking symmetry through the interface between two different materials. An interface between a ferromagnet and a strong spin-orbit metal gives rise to the necessary Dzyaloshinskii-Moriya interaction, even if both metals have inversion-symmetric lattices.

This book discusses the relevant fundamental concepts and results in this exciting field of research. Equal weight is dedicated on the realm of technological applications. The chapters start with a description of topologically stable structures in one-, two-, and three-dimensional space. The Thiele equation is derived from a fundamental micromagnetic description of statics and dynamics. A pure mathematical description of topology is included later for a rigorous definition of topological and metric spaces and compactness.

Realization of magnetic skyrmions in condensed matter physics propelled the development of numerous materials architectures and advances in experimental methods of characterization. Materials hosting magnetic skyrmions now range from bulk single crystals to synthetic architectures. High-resolution magnetic imaging has been at the center of skyrmion research and development. A comprehensive

description provided in this book helps the reader appreciate techniques that continue to make pioneering contributions in this field of research.

Intelligent device configurations employed to engineer skyrmion states in materials that would otherwise not accommodate such spin structures are discussed. In addition, exotic structures characterized by anisotropic Dzyaloshinskii-Moriya interaction and Ruderman-Kittel-Kasuya-Yosida interaction to host antiskyrmions and synthetic antiferromagnetic skyrmions are discussed. For instance, skyrmion stabilization and detection in antiferromagnets is at an early stage, facing many challenges ahead. Theoretical foundations however encourage further material development and characterization for the stabilization of skyrmions in antiferromagnetic structures. The community is increasingly active in this direction. Ferrimagnets represent another promising material platform for skyrmionics. Recent advances in imaging, writing, deleting, and electrical detection of ferrimagnetic skyrmions demonstrate their promising impact toward device technology.

An account on the statics and dynamics of magnetic skyrmions gives a glimpse in the key attributes of their technological potential. A detailed description of dynamics in the presence of thermal fluctuations is discussed in the light of recent proof of concept of skyrmion-based devices for probabilistic computing. Attention is given to the definition of the skyrmion configurational entropy based on the concept of Boltzmann order function, useful for the theoretical understanding of phase transitions in materials hosting skyrmions.

A direction highly relevant for applications is electrical manipulation. A strategy to nucleate skyrmions with electric currents is discussed, considering nucleation via spatial inhomogeneity, local injection of spin-transfer torque, and voltage-controlled magnetic anisotropy. Although the goal is the integration of magnetic tunnel junctions in multilayers hosting skyrmions, the topological Hall effect has proven an effective approach for electrical detection. Analysis of the topological Hall effect in the presence of magnetic skyrmions provides an up to date account of research and discusses pressing challenges. The discussion on the dynamics of skyrmions addresses also the so-called skyrmion Hall angle. Oblique trajectories followed by the skyrmion when moved by spin-orbit torques is a limiting factor in applications such as the racetrack memory. This has motivated the research community further to explore ferrimagnetic and antiferromagnetic materials as energy-efficient skyrmion hosts.

Skyrmion-based devices have the potential to store and process information at unprecedentedly small sizes and levels of energy consumption. The presence/absence of a skyrmion could serve as 1/0 in a data bit and multiple skyrmions can aggregate toward multivalued storage devices. The states of such devices can be modulated by an electric current, driving skyrmions in and out of devices in analogy to biological synapses. Researchers have already engineered interfacial skyrmions up to room temperature in magnetic multilayers, making their promise for future technologies more realistic. This offers an opportunity to bring topology into consumer-friendly, low-energy nanoscale electronics. The ability we have gained to engineer skyrmion-host platforms is propelling new technological opportunities. For example, conventional applications of skyrmions for the realization of memories, logic gates, transistors, and radio frequency circuits such as oscillators. The application of magnetic

---

skyrmions in unconventional computing is a tantalizing possibility including proposals for the realization of skyrmion-based memristors. One may also envisage energetically efficient neurons and synapses at device level toward low-power neuromorphics hardware.

It has been a pleasure to work with the co-authors and the Elsevier team. Their contributions have made possible the delivery of an inclusive description of the rapidly growing research field of magnetic skyrmions.

**Giovanni Finocchio**  
**Christos Panagopoulos**

# Mapping the magnetic field of skyrmions and spin spirals by scanning probe microscopy

4

Hans J. Hug<sup>a,b</sup>

<sup>a</sup>Empa, Swiss Federal Laboratories for Materials Science and Technology, Dübendorf, Switzerland, <sup>b</sup>Department of Physics, University of Basel, Basel, Switzerland

## 4.1 Introduction

Since the invention of the scanning tunneling microscope (STM) [1, 2], and the atomic force microscope [3] (scanning force microscope), a large family of scanning probe microscopes (SPMs) has been established for various applications. Among these are methods to map the stray field emanating from the surface of a sample, such as magnetic force microscopy (MFM) [4–7], scanning hall probe microscopy [8–11], scanning SQUID microscopy [12, 13], and more recently, nitrogen-vacancy (NV) microscopy [14]. To date, only MFM and NV center microscopy have been used for imaging the magnetic stray field generated by skyrmions and spin spirals.

Both the MFM and NV center microscopy do not directly measure the magnetic stray field, but a property related to it. Some calibration procedures are thus required to obtain one component of the stray field quantitatively from the measured property (see Sections 4.2.1, 4.2.4, 4.3.1, and 4.3.2). Note that it is sufficient to measure one component of the stray field in an  $xy$ -plane above the sample. The stray field components in the other directions can then be obtained from the measured component, because the magnetic field above the sample is a conservative field and can thus be derived as the negative gradient of a scalar magnetic potential (see Sections 4.2.4.2 and 4.3.2).

The information on the distribution of magnetic moments inside the sample that can be obtained from a measurement of the stray field remains, however, limited: different magnetization patterns (distribution of magnetic moments) can give rise to the same stray magnetic field above the sample. In the general case, and without additional knowledge on the magnetization structure, it is hence not possible to determine the three-dimensional (3D) magnetic moment distribution inside the sample from measurements of the stray field. Instead, stray fields calculated from candidate magnetization structures can be fitted to the measured stray field component to obtain the most likely magnetization pattern.

Because the stray field arising from a magnetic layer inside the sample can penetrate through nonmagnetic layers also (e.g., those used for oxidation protection or as a top electrode), MFM or NV microscopy can be used to study such samples. As typical

laboratory tools, these instruments have thus become methods of choice for a rapid analysis of the sample's micromagnetic state and its evolution with temperature, applied magnetic fields, and imposed electric currents. MFM or NV microscopy are thus well suited for the study of technologically relevant samples such as polycrystalline multilayers containing magnetic layers hidden below oxidation protection layers or other layers required for device operation.

## 4.2 Magnetic force microscopy methods

### 4.2.1 Magnetic force microscopy contrast formation

The MFM maps magnetic fields by a measurement of the interaction of the magnetic moment of the tip with the stray field of the sample. Consequently, a larger magnetic tip moment generates a larger signal and thus facilitates the measurement. However, the tip field can modify the micromagnetic state of the sample. Although this is often seen as a disadvantage of MFM compared to nonintrusive methods such as NV microscopy, it has been used to manipulate the micromagnetic state locally, that is, to generate a skyrmion state [15] or to write and delete single skyrmions [16]. In many cases, the modification of the micromagnetic sample state can be kept sufficiently small, such that it can be neglected. Often this is achieved by using tips with a smaller magnetic moment, for example, obtained by a reduction of the thickness of the ferromagnetic film deposited onto the otherwise nonmagnetic tip. Such a reduction of the tip moment, however, reduces the measured signal such that the MFM must thus be made more sensitive. In an optimum case, that is, if the control electronics is optimized, the sensitivity of an MFM is given by the thermal noise of the cantilever, which is described by [17]

$$F|_{\min} = \sqrt{\frac{4\pi k_B T c_L B}{\omega_0 Q}}, \quad (4.1)$$

where  $F|_{\min}$  and  $\left. \frac{dF_z}{dz} \right|_{\min} = \frac{1}{A_{\text{rms}}} \cdot F|_{\min}$  are the minimally measurable force and  $z$ -derivative of the  $z$ -component of the force, respectively,  $A_{\text{rms}}$  is the rms oscillation amplitude of the cantilever,  $k_B = 1.38 \times 10^{-23} \text{ JK}^{-1}$  is the Boltzmann constant,  $T$  is the temperature,  $c_L$  is the stiffness of the cantilever,  $B$  is the measurement bandwidth,  $\omega_0 = 2\pi f_0$  with  $f_0$  being the free resonance frequency of the cantilever, and  $Q$  is the mechanical quality factor of the cantilever. The latter is limited by various effects, such as the viscous drag of the cantilever motion in air but also by coatings deposited onto the cantilever surface. Hence, operating the MFM in vacuum (even in moderate vacuum, e.g.,  $10^{-6}$  mbar) removes the viscous drag from the environment and consequently reduces the noise. A further increase of the quality factor can be obtained by a dedicated engineering of the coatings on the cantilever, required, for example, to enhance the optical reflectivity of cantilever for optical detection of the cantilever position, and to make the tip sensitive to magnetic stray fields. Typical quality factors

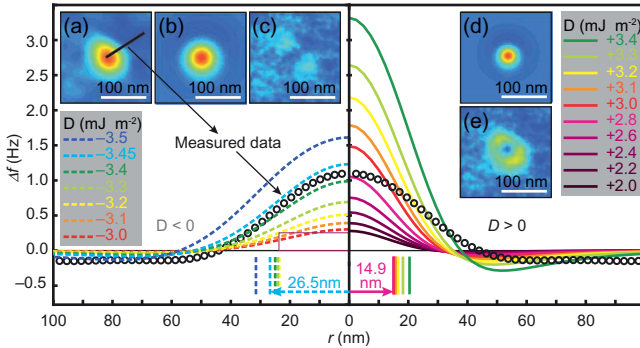


**Fig. 4.18** (a) MFM image of a skyrmion. (b) Simulation of the MFM image using a  $D_{\text{film}} < 0$  chosen to match the experimental peak contrast as per panel (a). (c) The difference image (a and b) reveals that the simulated Skyrmion MFM image matches the measured image well. (d) Simulation of the MFM image using a  $D_{\text{film}} > 0$  chosen to match the experimental peak contrast as per panel (a). (e) The difference image reveals that the modeled skyrmion MFM image matches the center contrast of the measured skyrmion but not the width of the measured skyrmion. The cross section calculated for  $D_{\text{film}} = -3.45 \text{ mJ m}^{-2}$  nicely match that from the measurement, while all cross sections for  $D_{\text{film}} > 0$  fail to match the measured contrast. Modified from M.A. Marioni, M. Penedo, M. Bacani, J. Schwenk, H.J. Hug, Halbach effect at the nanoscale from chiral spin textures, *Nano Lett.* 18 (4) (2018) 2263–2267. Copyright 2020. American Chemical Society.

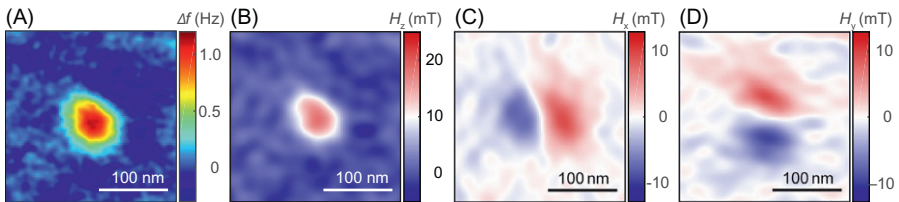


**Fig. 4.19** (A) MFM image of a skyrmion. (B)  $z$ -Component of the magnetic field of the skyrmion obtained from (A) by deconvolution with the response function of the MFM tip. (C and D)  $x$ - and  $y$ -component of the magnetic field of the skyrmion obtained from the  $z$ -component showed in (B). Modified from M.A. Marioni, M. Penedo, M. Bacani, J. Schwenk, H.J. Hug, Halbach effect at the nanoscale from chiral spin textures, *Nano Lett.* 18 (4) (2018) 2263–2267. Copyright 2020. American Chemical Society.

for example,  $H_z$  in a plane above the sample surface (Fig. 4.19B).  $H_z(x, y)$  can, for example, be obtained from the deconvolution of the measured MFM image of a skyrmion (Fig. 4.19A). The other field components, for example,  $H_x$  (Fig. 4.19C) or  $H_y$  (Fig. 4.19D) can then be obtained from  $H_z$ . Note that a similar procedure was used to determine all field components from an  $H_z(x, y)$  image measured by NV microscopy [48] and Section 4.3.

## 4.3 NV-center microscopy

### 4.3.1 NV-center microscopy contrast formation

While MFM is a robust lab tool to image stray fields emanating from magnetic sample surfaces with high spatial resolution at various temperatures and in fields of up to several Tesla and can even perform quantitative field measurements of all vector components of the magnetic field (see, e.g., Marioni et al. [23] and Fig. 4.19), it relies on the interaction of a ferromagnetic tip with the sample stray field. The ferromagnetic tip inevitably generates a stray field that can perturb the micromagnetic state of the sample, particularly if magnetically soft samples are imaged with large magnetic moment tips (which are often used to compensate, e.g., for the lack of sensitivity if an MFM is operated under ambient conditions). Further, the MFM tip is a finite-size nanoscale object, inherently limiting the lateral resolution to about 10 nm to date in the best cases [29].

In the quest of improving the lateral resolution and sensitivity of field mapping methods, Chernobrod and Bergman [14], based on earlier ideas of Sekatskii and Letokov [51], proposed the use of single-spin nanoscale quantum sensors. The main advantages are that the sensor has atomic-scale dimensions and can offer excellent field sensitivity. Since the year 2006, the research community working with optical magnetometry [52, 53] realized that a nitrogen-vacancy (NV) center in diamond exhibits the physical properties that make it a nearly ideal candidate to realize the ideas of Chernobrod and Bergman [14]. The proposals and first proof-of-concept experiments as well as various experimental and theoretical work are reviewed in Ref. [54].

An NV center consists of a substitutional nitrogen atom (N) and a vacancy (V) at one of the nearest-neighbor sites of the diamond crystal lattice (Fig. 4.21A). Note that two different forms of the NV defect exist: a neutral state and a negatively charged state, with only the latter showing physical properties suitable for magnetometry applications [54]. Fig. 4.21B shows the energy level diagram of a (negatively charged) NV center, including the relevant optical and microwave transitions between the levels that are used for the implementation of magnetometry applications. The  ${}^3A_2$  ground level is a spin-triplet state, whose sublevels are split by spin-spin interaction into a singlet state of spin projection  $m_s = 0$ , and a doublet with  $m_s = \pm 1$  that are separated by  $D = 2.87$  GHz in the absence of a magnetic field (indicated by the blue arrow in Fig. 4.21B). A magnetic field  $B_{\text{NV}}$  applied along the quantization axis of the NV center  $\mathbf{n}_{\text{NV}}$  (the direction of the NV axis) leads to a splitting of the  $m_s = \pm 1$  states by  $2g\mu_B B_{\text{NV}}$ , where  $g \approx 2$  is the electron g-factor. Using green laser light, the defect can be optically excited through spin-conserving transitions to a  ${}^3E$  excited level, which is also a spin triplet. From this excited level, relaxation can either occur through the same radiative transition generating a broadband red photoluminescence (PL), or through a second path involving a nonradiative intersystem crossing (ISC) to singlet states. The nonradiative ISCs to the  ${}^1E$  singlet state are found to be strongly spin selective, with rates from the  $m_s = \pm 1$  states being much higher than from the  $m_s = 0$  states. Conversely, the lowest  ${}^1A_1$  singlet state to the ground state preferentially decays into

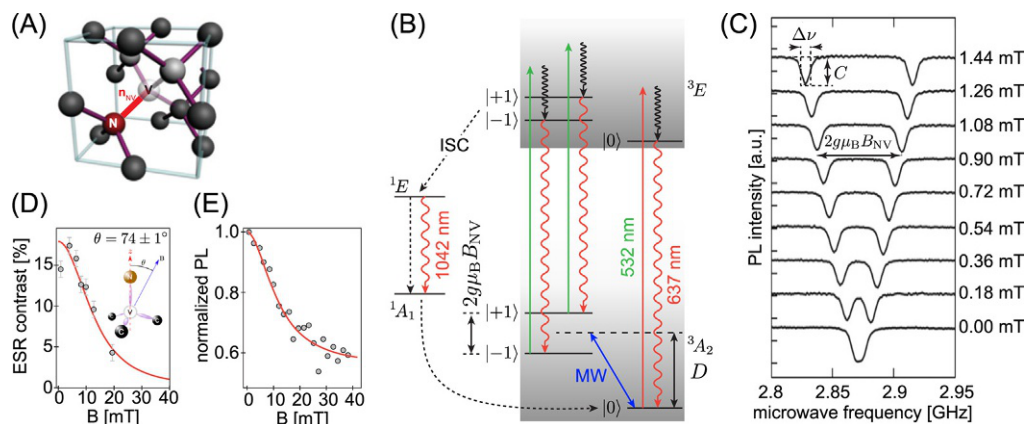


**Fig. 4.21** (A) Atomic structure of the NV defect in diamond. (B) Energy-level scheme. The notation  $|i\rangle$  denotes the state with spin projection  $m_s = i$  along the NV defect axis  $\mathbf{n}_{NV}$ . Spin-conserving optical transitions from the  $^3A_2$  spin-triplet ground state to the  $^1E$  excited state are shown with the *green solid arrows*. Such transitions are efficiently excited through nonresonant green illumination on the phonon sidebands. The *dashed arrows* indicate spin selective intersystem crossing (ISC) involving the singlet states  $^1E$  and  $^1A_1$ . The infrared (IR) transition occurring at 1042 nm between the singlet states is also shown. (C) Optically detected electron spin resonance (ESR) spectra recorded for different magnetic field magnitudes applied to a single NV defect in diamond. The ESR transitions are shifted owing to the Zeeman effect, thus providing a quantitative measurement of the magnetic field projection along the NV defect quantization axis. These spectra are recorded by monitoring the NV defect PL intensity while sweeping the frequency of the microwave (MW) field. Spectra for different magnetic fields are shifted vertically for clarity. (D) ESR contrast and (E) normalized PL intensity as a function of magnetic field amplitude applied with an angle  $\theta = 74 \pm 1$  degrees with respect to the NV defect axis  $\mathbf{n}_{NV}$ . The *solid line* is the result of a rate equation model developed in Ref. [55]. Modified from L. Rondin, J.P. Tetienne, T. Hingant, J.F. Roch, P. Maletinsky, V. Jacques, Magnetometry with nitrogen-vacancy defects in diamond, Rep. Prog. Phys. 77 (5) (2014). Copyright 2020. Institute of Physics Publishing, Great Britain.

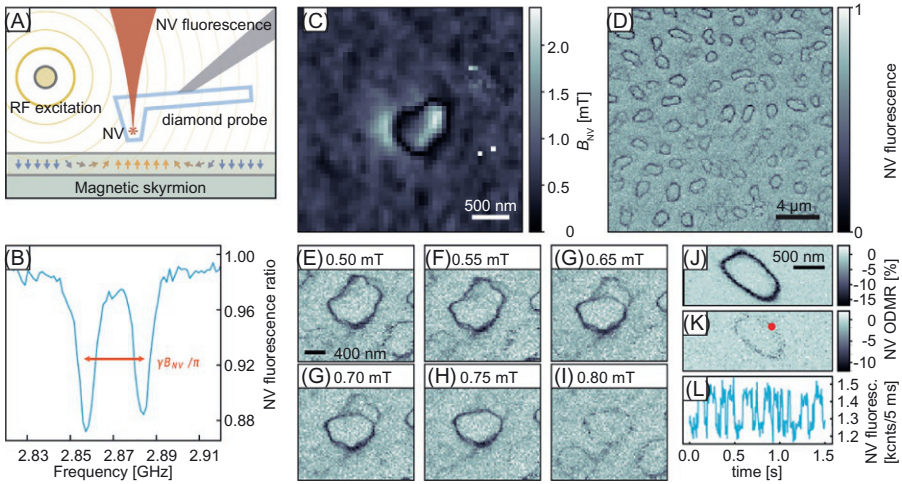


**Fig. 4.23** (A) Diagram of the experimental setup. A single-crystal diamond probe containing a single NV center near the apex of its tip is scanned above the multilayer sample. Simultaneous optical and RF excitation of the NV gives an ESR signal (B), which is used to measure the stray magnetic field at each position in the scan. (B) Example of an NV ESR signal: The NV fluorescence rate decreases when applied microwaves are on resonance with either of the NV's two spin transitions ( $m_s = 0 \rightarrow +1$  and  $m_s = 0 \rightarrow -1$ ). The splitting of the two peaks is used to calculate  $B_{NV}$ , the magnetic field along the NV center axis. Plotted is the ratio of the NV fluorescence to its off-resonant value. (C) NV magnetic image of a skyrmion bubble with an external magnetic field of 1 mT perpendicular to the film plane. (D) Magnetic contour image with applied microwave frequency equal to 2.870 GHz and with 0.65 mT field perpendicular to the film plane. (E–I) 2.870 GHz contour images of a skyrmion bubble, each labeled by the corresponding  $B_{ext}$  applied during that scan. As  $B_{ext}$  increases, a section of the domain wall evolves into a bistable configuration, seen most clearly in (F) and (G) with 0.65 and 0.7 mT, respectively. (J) 2.870 GHz contour image of the skyrmion bubble at  $B_{ext} = 0.92$  mT. As the field is increased to 0.95 mT, the bubble state becomes unstable and switching between the saturated and bubbles states is observed as a decrease in the NV ESR contrast. (K) The NV fluorescence collected in 5 ms bins when fixing the NV location at the position indicated by the red dot in (K) and fixing the drive microwave frequency at 2.871 GHz. (L) The NV fluorescence collected in 5 ms bins when fixing the NV location at the position indicated by the red dot in (B) and fixing the drive microwave frequency at 2.871 GHz. A characteristic hopping frequency of 14 Hz is measured over the full 30 s measurement window.

Modified from A. Jenkins, M. Pelliccione, G. Yu, X. Ma, X. Li, K.L. Wang, A.C.B. Jayich, Single-spin sensing of domain-wall structure and dynamics in a thin-film skyrmion host, Phys. Rev. Mater. 3 (8) (2019) 083801. Copyright 2020. American Physical Society.

dependence of the magnetic structures on the applied field (Fig. 4.23D–K). Dark contours in the measured image then correspond to locations where the applied microwave frequency is in resonance with the  $m_s = 0$  to  $m_s = \pm 1$  transitions and are thus (in a first-order approximation) contours of constant magnetic field along the NV center quantization axis. Fig. 4.23D shows a such a magnetic contour image of several skyrmion bubbles recorded with an applied microwave frequency equal to

# Scanning probe microscopy methods for imaging skyrmions and spin spirals with atomic resolution

5

Hans J. Hug<sup>a,b</sup>

<sup>a</sup>Empa, Swiss Federal Laboratories for Materials Science and Technology, Dübendorf, Switzerland, <sup>b</sup>Department of Physics, University of Basel, Basel, Switzerland

## 5.1 Introduction

Since its invention, the scanning tunneling microscope (STM) [1, 2] has become an established surface science tool. In an STM, a metallic tip is brought into a close proximity to a conducting sample. At a sufficiently small tip-sample distance, typically below 1 nm, a tunnel current can flow, which depends on the applied bias,  $U$ , on the electronic states of the tip and sample, and exponentially on the tip-sample distance. The tunnel current decays by about one order of magnitude for an increase of the tip-sample distance by 1 Å. This rapid decay ultimately permits to image surfaces with atomic resolution, in spite of the radii of several tens of nanometers typical for STM tips, because most of the tunneling current flows through the apex atom.

An STM can be operated in an imaging mode where the tip-sample distance is adjusted by a feedback such that the measured tunnel current remains constant. Alternatively, the tip can be scanned at constant average height, or with a slow distance feedback, and the variation of the tunneling current arising from the local topography or spatial variations of the local density of states (DOS) can be mapped, provided that the topography is sufficiently small to avoid a tip-sample crash. To explore the electronic states, the dependence of the tunneling current  $I$  on the sample bias  $U$  can be explored. For this, either the dependence  $\frac{dI}{dU}$  on the sample bias  $U$  at a selected tip position  $\mathbf{R}_t$ , or its dependence  $\frac{dI}{dU}$  on the tip position  $\mathbf{R}_t$  at a selected bias  $U$  are recorded to either locally map the electronic states or acquire a spectroscopic image of the sample. Using magnetic tips, the current can become spin-polarized, and thus probe local spin-polarized states with atomic-scale resolution. First, spin-polarized scanning tunneling microscopy (SP-STM) experiments have been reported by Wiesendanger et al. [3, 4]. Sections 5.2.1 and 5.2.1.1–5.2.1.3 review magnetic contrast formation in STM, while Sections 5.2.2.1 and 5.2.2.2 are devoted to the imaging of spin spirals and skyrmions and their manipulation.

With the invention of the atomic force microscope (AFM) [5] or more generally the scanning force microscope (SFM), a scanning probe microscopy tool to image

insulating sample surfaces with highest lateral resolution became available. In their publication, Binnig et al. [5] presented scanlines acquired on an  $\text{Al}_2\text{O}_3$  surface displaying features having a width of about 3 nm. Images showing structures with atomic-scale periodicities were presented a few years later by various groups [6–9], but it was soon recognized that the images show atomic periodicity. However, atomic-scale defects or unit cell steps with atomic extension perpendicular to the step edge were never observed. First images with true atomic resolution were obtained almost a decade after the invention of the AFM by Giessibl [10], Kitamura and Iwatsuki [11], and by the Morita group by Ueyama et al. [12] and Sugawara et al. [13]. For this, the tip is brought into close vicinity of the sample surface such that short-range forces arising from incipient chemical bonds between the tip apex atom and surface atoms occur (see Ref. [14] for a review of the earlier work on AFM with atomic resolution). Since 1995, various semiconducting, metallic, and insulating samples have been imaged with atomic resolution. More recently, the controlled functionalization of the tip, either by a CO molecule [15] or by an O atom [16], has become a popular technique to image organic molecules on surfaces.

In case the tip is covered with a magnetic material, the instrument becomes sensitive to magnetic stray field emanating from the sample surface (see Chapter 4). However, if the apex atom of an AFM tip coated with a ferromagnetic or antiferromagnetic material is approached sufficiently close to the surface of a magnetic sample, the interatomic chemical bonding energy depends on the relative spin orientation of the tip apex and surface atom. Consequently, a magnetic exchange force can be measured and in the best case a magnetic image with atomic resolution can be obtained. The concept of magnetic exchange force microscopy (MExFM) was first demonstrated by Kaiser et al. [17]. Section 5.3.1 gives a short introduction into the MExFM concepts, while Section 5.3.2 reviews the work performed with MExFM techniques to assess spin spirals and skyrmions.

Out of all experimental methods used for skyrmion imaging, SP-STM and MExFM offer the highest spatial resolution (down to the atomic scale). However, in case of the SP-STM, a magnetic contrast can occur only if the electrons can tunnel into the magnetic layer of the sample. Similarly, the MExFM provides a magnetic contrast only if a spin-dependent exchange force between the tip apex atom and atoms on the surface of the sample occurs. Hence, both methods can only be applied, if the magnetic layer is accessible at the surface of the sample. Also, disentangling magnetic and topographical contrast becomes challenging on samples with a roughness on the scale of a few nanometers, which is typical for polycrystalline samples. This then excludes samples where the magnetic layers are covered by other layers, for example, for oxidation protection or by electrodes to introduce electrical currents or perform a readout of the spin texture. Furthermore, almost all reported SP-STM and MExFM experiments on systems with skyrmions have been carried out at low temperatures. These are presumably required to obtain the stability needed to perform such measurements, but also because the thermal stability of atomic-scale spin textures is limited [18]. Thus, imaging technically relevant samples by SP-STM or MExFM remains challenging and has not yet been reported, apart from a nanoskyrmion lattice observed in a Si-wafer-based multilayer system consisting of an Fe ML deposited onto a single-crystalline Ir/YSZ/Si (111) substrate inside the SP-STM system [19].

However, in contrast to SPM methods mapping the stray field, SP-STM allows to map the topography and the electronic surface states of a sample with atomic resolution. Moreover, it can also provide spectroscopic information, and different contrast mechanisms can be advantageously combined to obtain local information on spin-orbit coupling and the local degree of the spin noncollinearity. SP-STM methods hence provide data sets with atomic-scale lateral resolution allowing a direct comparison with results from *ab initio* calculations and other spin-resolved atomic-scale modeling work. With this, SP-STM and MExFM methods are ideally suited to study fundamental phenomena in otherwise well-defined single-crystalline systems.

## 5.2 Scanning tunneling microscopy methods

### 5.2.1 Scanning tunneling microscopy contrast formation

If a magnetic sample is studied with an STM using a spin-polarized tip, a magnetic contrast can arise since the tip and sample density of states are spin-dependent (Fig. 5.1A) [20, 21]. To date, tips providing a spin polarization are typically prepared by depositing a few monolayers (MLs) of a ferromagnetic or antiferromagnetic materials onto an etched tungsten tip that has been heated up to 2200 K in UHV to form a semisphere with a radius of about 500 nm. Coating the W tip with 3–5 MLs of Fe results in a tip with an in-plane magnetization, while W tips coated with 7–9 MLs Gd or 10–15 MLs of Gd<sub>90</sub>Fe<sub>10</sub>, or  $\pm 35$  MLs of Cr show an out-of-plane magnetization [20, 22]. Note that the Cr-coated tip is antiferromagnetically ordered, which minimizes the stray field of the tip. Alternatively, bulk antiferromagnetic Cr tips have been used [23]. The magnetic moment direction of the tip apex atom of a bulk Cr tip is along an arbitrary direction, but Schlenhoff et al. [23] showed that it can be changed by

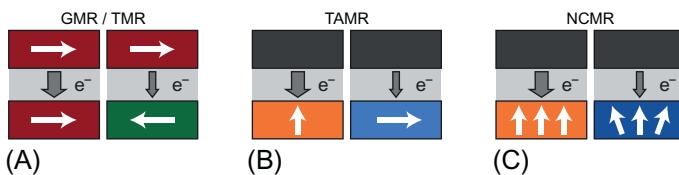


**Fig. 5.1** Magnetoresistive effects in tunneling junctions. (A) Sketch of the tunneling magnetoresistance (TMR) effect, in which two magnetic electrodes are separated by an insulator or vacuum. (B) The tunneling anisotropic magnetoresistance (TAMR) effect does not require a magnetic sensor electrode (tip). The effect arises from the intrinsic spin-orbit coupling (SOC) within the magnetic layer giving a different conductance for an out-of-plane and in-plane magnetization of the sample. (C) The noncollinear magnetoresistance (NCMR) effect arises from a sample with a noncollinear spin texture giving rise to a contrast if the degree of the noncollinearity changes.

Modified from C. Hanneken, F. Otte, A. Kubetzka, B. Dupé, N. Romming, K. von Bergmann, R. Wiesendanger, S. Heinze, Electrical detection of magnetic skyrmions by tunnelling non-collinear magnetoresistance, *Nat. Nanotechnol.* 10 (12) (2015) 1039–1042. Copyright 2020. Springer Nature.

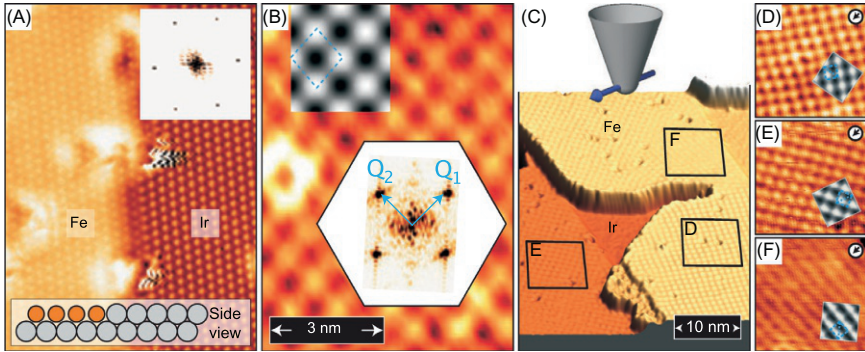


**Fig. 5.9** (A) Atomic-resolution STM image of the pseudomorphic hexagonal Fe layer at an Ir step edge. *Upper inset*: The FFT. *Lower inset*: A side view of the system (tunnel parameters  $U = +5$  mV,  $I = 30$  nA). (B) SP-STM image of the Fe ML on Ir(111) with a magnetic tip sensitive to the out-of-plane component of magnetization (Fe-coated W tip,  $B = +2$  T along the tip axis,  $U = +50$  mV,  $I = 0.5$  nA): *bright (dark) spots* indicate areas with magnetization parallel (antiparallel) to the tip magnetization. *Upper inset*: simulated SP-STM image of the nanoskyrmion with out-of-plane magnetic tip. *Lower inset*: FT of the experimental SP-STM image shown in the two-dimensional Brillouin zone. (C) Three-dimensional representation of a sample area with all three possible rotational magnetic domains measured with a tip sensitive to the in-plane component of magnetization as shown (Fe-coated W tip,  $U = +5$  mV,  $I = 0.2$  nA, sketched tip magnetization axis inferred from comparison to simulated SP-STM images). (D–F) Closer views of the three rotational domains indicated by squares in (C) displayed with a  $z$ -scale of 23 pm; the tip magnetization is indicated by the *arrows*. *Insets*: simulations of SP-STM measurement of the nanoskyrmion with this tip magnetization.

Modified from S. Heinze, K. von Bergmann, M. Menzel, J. Brede, A. Kubetzka, R. Wiesendanger, G. Bihlmayer, S. Blügel, Spontaneous atomic-scale magnetic skyrmion lattice in two dimensions, *Nat. Phys.* 7 (9) (2011) 1–6. Copyright 2020. Springer Nature.

A spin-spiral and a more conventional skyrmion phase was observed by Romming et al. [43] in a PdFe bilayer on Ir(111). The SP-STM data acquired at zero field with a bulk Cr spin-polarized tip revealed a spin-spiral magnetic ground state with a period of 6–7 nm (Fig. 5.10A and B). When a field of 1 T is applied perpendicular to the sample surface, skyrmions coexist with spin-spiral domains (Fig. 5.10D), whereas at 1.4 T a slightly disordered hexagonal skyrmion lattice is observed (Fig. 5.10E). Higher fields finally lead to a homogeneous ferromagnetic state (not shown).

In later work, Romming et al. [38] presented a field-dependent study of the skyrmion size and shape. Again bulk Cr tips were used which permit to change the magnetic moment direction of the apex atom by voltage pulses or by gently touching the sample surface [23]. Moreover, the magnetic moment direction remains unaffected by an applied field, making such tips ideal for field-dependent studies.

Fig. 5.11A shows a schematical view of the clockwise spin texture of a skyrmion in a RhFe bilayer deposited on the Ir(111) single-crystalline surface. An SP-STM image recorded with a tip sensitive to the out-of-plane direction is shown in Fig. 5.11B. In a down field, the skyrmion core magnetization is up, generating a positive  $\Delta z$  (blue)

of the magnetic film. In order to disentangle an SOT effect from a switching process governed solely by the electric field, nonspin-polarized W tips were used. The bean-shaped skyrmions can still be imaged because of the NCMR effect, and reproducibly be erased and written by choosing the appropriate direction of the electric field. The authors concluded that for an electric field pointing toward the sample surface (negative sample bias as shown in Fig. 5.18A), an inward relaxation of the Fe atomic nuclei occurs which leads to an increase of the magnetic exchange energy and, consequently, to a preference of the ferromagnetic state, that is, to an annihilation of a skyrmion.

## 5.3 Magnetic exchange force microscopy

### 5.3.1 Contrast mechanism

Atomic force microscopy measures the force acting on the tip that is brought into close vicinity of the sample surface. Typically, an AFM or SFM is operated in a dynamic mode, where shifts of the cantilever resonance frequency,  $\Delta f$ , arising from the  $z$ -derivative of the  $z$ -component of the force weighted over the tip-sample distance range covered by the oscillation of the cantilever tip [14], are measured. It has been demonstrated that AFM can obtain (true) atomic resolution provided, that the tip apex atom approaches the surface atoms to a distance sufficiently small that short range forces, arising from a chemical interaction between the tip apex atom and individual surface atoms, can occur (see Ref. [14] for a review of the earlier work on AFM with atomic resolution).

On magnetic samples and when using a magnetic tip material, the interatomic chemical bonding energy also depends on the relative spin orientation of the two interacting atoms. Consequently, the force between tip apex atom having a fixed spin direction arising from a spin-up surface atom is expected to be different from that of a spin-down surface atom. The concept of magnetic exchange force microscopy (MExFM) was first demonstrated by Kaiser et al. [17] who used an Fe-coated cantilever tip in a field of 5 T to image rows of antiferromagnetically ordered Ni spins of opposite orientation on the surface of a NiO(001) single crystal (Fig. 5.19). In a later work, Schmidt et al. [54] also resolved the antiferromagnetic structure of an Fe monolayer on W(001). While Kaiser et al. [17] and Schmidt et al. [54] both relied on an AFM equipped with a microfabricated cantilever, MExFM contrast on the NiO(001) surface has also been demonstrated by tuning fork AFM [55]. Note that chemical interaction forces (including the spin-dependent part) are much larger than typical magnetic dipole forces measured by MFM such that the inferior force or force gradient sensitivity of the tuning forks compared to that of cantilevers is not relevant. On the contrary, when operated with small oscillation amplitudes comparable to the range of the interatomic forces, tuning fork-based AFMs can easily obtain a signal-to-noise ratio that can surpass that of cantilever AFM operated with nanometer-sized oscillation amplitudes [55–57]. Moreover, the high spring constant of a tuning fork and the mesoscopic metal tip attached to it, considerably facilitated measurements that

### 5.3.2 Imaging spin-spiral states and skyrmion by MExFM

A first application of MExFM for imaging skyrmions was presented by Grenz et al. [63] using a cantilever-type AFM, and just 2 months later by Hauptmann et al. [56] applying a combination of SP-STM and MExFM (abbreviated SPEX) with a tuning-fork-based AFM. The studied system was an Fe monolayer on Ir(111) previously studied by SP-STM that shows an incommensurate square nanoskyrmion lattice at zero field (Fig. 5.9) arising from a four-spin interaction and interfacial DMI [37]. Fig. 5.20A shows an overview noncontact AFM topography image of the Fe/Ir(111) sample with a coverage of 0.7 ML of Fe measured with a frequency shift kept constant at  $-12\text{Hz}$  using a cantilever with a stiffness  $k_c = 147.1\text{N m}^{-1}$  with an oscillation amplitude  $A = 2.3\text{nm}$ , at a sample bias of  $U = +0.1\text{V}$  applied to minimize the electrostatic tip-sample force. Fig. 5.20B shows a frequency shift ( $\Delta f$ ) atomic resolution image recorded with a cantilever with a stiffness  $k_c = 148.3\text{N m}^{-1}$  with an oscillation amplitude  $A = 1.2\text{nm}$ , and at a sample bias of  $U = +0.9\text{V}$ , acquired by scanning at constant height parallel to the surface. To make the cantilever tip magnetically sensitive the super-sharp Si tips were coated by a Ti adhesion layer of several nanometers, followed by an Fe layer of similar thickness. For magnetic imaging, the tip was again scanned at constant height, and a field of  $4\text{T}$  was used to obtain an out-of-plane magnetization of the tip apex. The data shown in Fig. 5.20C and the Fourier-filtered image (Fig. 5.20D) reveal both the hexagonal atomic structure and the incommensurate nanoskyrmion square lattice. In contrast to STM, MExFM facilitates the determination of the relation between the atomic and magnetic structure, because both of these data set can be simultaneously measured.

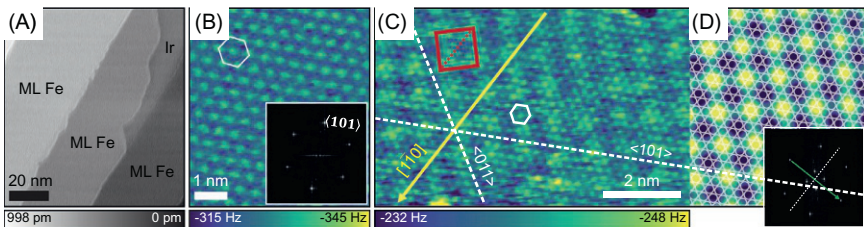


**Fig. 5.20** (A) Topography of 0.7 ML of Fe on Ir(111) recorded by noncontact AFM. (B) Atomic resolution frequency-shift image recorded at constant height with a nonmagnetic tip (*inset*: Fourier transform). (C) MExFM image of the 0.7 ML of Fe on Ir(111) recorded with an Fe-coated tip in constant-height mode ( $A = 0.8\text{ nm}$ ,  $k_c = 147.2\text{ N m}^{-1}$ ,  $U = +1.1\text{ V}$ ). An applied magnetic field of  $B = 4\text{ T}$  ensures an out-of-plane magnetized tip. In addition to the hexagonal atomic structure (white hexagon), the magnetic structure of the nanoskyrmion lattice (*red square*) is visible as well. (D) Fourier-filtered image generated from (C) by taking only the atomic and magnetic peaks of the 2D FT. The atomic lattice has been reproduced by a hexagonal arrangement of *white circles*. *Inset*: the 2D FT of the raw image data clearly reveals that the atomic and magnetic structure are incommensurate.

Modified from J. Grenz, A. Köhler, A. Schwarz, R. Wiesendanger, Probing the nano-skyrmion lattice on Fe/Ir(111) with magnetic exchange force microscopy, Phys. Rev. Lett. 119 (4) (2017) 047205. Copyright 2020. American Physical Society.

Magnetic skyrmions are particle-like objects described by localized solutions of nonlinear partial differential equations. Up until a few decades ago, it was believed that magnetic skyrmions only existed in condensed matter as short-term excitations that would quickly collapse into linear singularities. The contrary was proven theoretically in 1989 and experimentally in 2009. It is now known that skyrmions can exist as long-living metastable configurations in low-symmetry condensed matter systems with broken mirror symmetry, increasing the potential applications possible. *Magnetic Skyrmions and Their Applications* delves into the fundamental principles and most recent research and developments surrounding these unique magnetic particles.

Despite achievements in the synthesis of systems stabilizing chiral magnetic skyrmions and various experimental investigations and numerical calculations, there have not been many summaries of the fundamental physical principles governing magnetic skyrmions or integrating those concepts with methods of detection, characterization, and potential applications. This book delivers a coherent and comprehensive overview on the current knowledge and potential applications of magnetic skyrmions in magnetic materials and device applications.

First, the book reviews key concepts such as topology, magnetism, and materials for magnetic skyrmions. Then, characterization methods, physical mechanisms, and emerging applications are discussed.

### Key Features

- Covers background knowledge and details the basic principles of magnetic skyrmions, including materials, characterization, statics, and dynamics
- Reviews materials for skyrmion stabilization, including bulk materials and interface-dominated multilayer materials
- Describes both well-known and unconventional applications of magnetic skyrmions, such as memristors and reservoir computing

**Giovanni Finocchio** received his PhD in advanced technologies for optoelectronics, photonics, and electromagnetic modeling from the University of Messina in 2005, where he is now Associate Professor of Electrical Engineering and director of PETAscale computing and SPINtronic laboratory. He has coauthored more than 180 articles and given more than 100 invited talks on magnetic-related topics. He is Chair of the Italy chapter of IEEE Magnetics Society since 2019, and AdCom member of IEEE Magnetic Society for 2020–2022.

**Christos Panagopoulos** received his PhD from the University of Cambridge (Trinity College) in 1997. He is a professor of physics at Nanyang Technological University and an investigator at the National Research Foundation, both in Singapore. His research connects the quantum architecture of materials directly with new quantum device responses. He has published more than 100 articles in this field of research and presented more than 200 invited lectures at international conferences and universities.

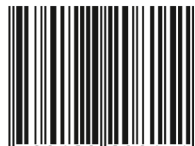


**WP**

WOODHEAD  
PUBLISHING

An imprint of Elsevier  
[elsevier.com/books-and-journals](https://www.elsevier.com/books-and-journals)

ISBN 978-0-12-820815-1



9 780128 208151